Nuclear Engineering and Technology 56 (2024) 846–854

Contents lists available at ScienceDirect

Nuclear Engineering and Technology

journal homepage: www.elsevier.com/locate/net

Original Article

# Development of FEMAXI-ATF for analyzing PCMI behavior of SiC cladded fuel under power ramp conditions

Yoshihiro Kubo *, Akifumi Yamaji

*Graduate School of Advanced Science and Engineering, Waseda University, 3-4-1, Okubo, Shinjuku-ku, Tokyo, 169-8555, Japan*

ARTICLE INFO

*Keywords:*
Accident tolerant fuel (ATF)
SiC cladded fuel
PCMI
Fuel performance analysis
FEMAXI-ATF
Power ramp

ABSTRACT

FEMAXI-ATF is being developed for fuel performance modeling of SiC cladded UO2 fuel with focuses on modeling pellet-cladding mechanical interactions (PCMI). The code considers probability distributions of mechanical strengths of monolithic SiC (mSiC) and SiC fiber reinforced SiC matrix composite (SiC/SiC), while it models pseudo-ductility of SiC/SiC and propagation of cladding failures across the wall thickness direction in deterministic manner without explicitly modeling cracks based on finite element method in one-dimensional geometry. Some hypothetical BWR power ramp conditions were used to test sensitivities of different model parameters on the analyzed PCMI behavior. The results showed that propagation of the cladding failure could be modeled by appropriately reducing modulus of elasticities of the failed wall element, so that the mechanical load of the failed element could be re-distributed to other intact elements. The probability threshold for determination of the wall element failure did not have large influence on the predicted power at failure when the threshold was varied between 25 % and 75 %. The current study is still limited with respect to mechanistic modeling of SiC failure as it only models the propagation of the cladding wall element failure across the homogeneous continuum wall without considering generations and propagations of cracks.

## 1. Introduction

Developing accident tolerant fuel (ATF) with improved tolerance to severe accident of light water reactors has become an important issue since the accident involving hydrogen explosions at the Fukushima Daiichi nuclear power station in 2011. The major research and development activities on ATFs are ongoing worldwide for developing ATFs with the standard UO2 fuel pellets and advanced fuel claddings with improved oxidation resistance against high temperature steam to suppress hydrogen and heat generation under severe accident conditions [1]. Among different cladding candidates, such as Cr-coated Zircaloy (Zry) and advanced stainless steel, silicon carbide (SiC) is known to show outstanding oxidation resistance against high temperature steam as well as excellent irradiation tolerance [2].

SiC generally shows large uncertainties in mechanical strengths, such as the proportional limit stress (PLS) and ultimate tensile strength (UTS) and large volumetric swelling by neutron irradiation, which also leads to substantial reduction in thermal conductivity. To utilize such material, the SiC cladding normally consists of two or more layers of different structures. Namely, the monolithic chemical vapor deposition (CVD) SiC (mSiC) and chemical vapor infiltration (CVI) SiC fiber reinforced SiC matrix composites (SiC/SiC) [3]. The high-density mSiC layer renders a primary retention of fission products (FPs) but cannot be used on its own as a cladding, because of its poor ductility. SiC/SiC, on the other hand, gains some pseudo-ductility due to the fiber reinforced structure, but loses its capability to retain fission gases when the stress exceeds the PLS and microcracks spread throughout the matrix.

To evaluate fuel performance of such SiC cladded fuel rods (SiC-UO2), extensive studies have been carried out with regard to evaluations of stress, strain and failure probabilities of the cladding wall induced by mismatch of the thermal expansion and irradiation swelling across the cladding wall [4]. It has been shown that different operation conditions, including accident conditions such as loss of coolant accident (LOCA), lead to different stress/strain in the cladding wall [5]. Influence of the anisotropy of SiC/SiC on stress and strain distributions in the cladding wall has also been studied [6]. However, pellet-cladding mechanical interaction (PCMI) was not considered in these studies.

In the meantime, development of FEMAXI-ATF fuel performance analysis code for modeling SiC-UO2, including the PCMI characteristics, has been initiated at Japan Atomic Energy Agency (JAEA) [7] based on

* Corresponding author.
*E-mail address:* ykubo@asagi.waseda.jp (Y. Kubo).

https://doi.org/10.1016/j.net.2023.10.014
Received 8 June 2023; Received in revised form 5 September 2023; Accepted 15 October 2023
Available online 18 October 2023

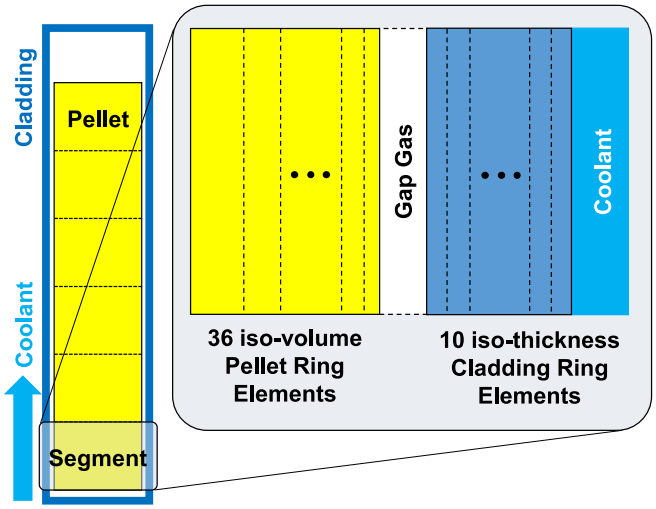


**Fig. 1.** Basic calculation geometry of FEMAXI.

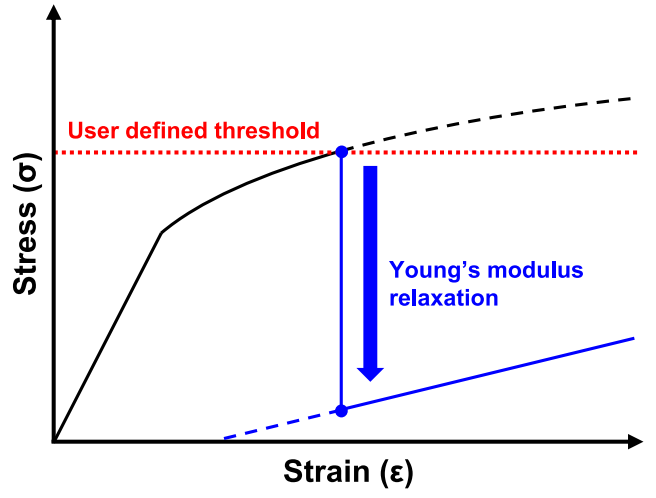


**Fig. 2.** Stress-strain model concept of FEMAXI-ATF to consider pseudo-ductility and failure of SiC/SiC.

the well-established experience of the FEMAXI-7 fuel performance analysis code [8]. The code treats the cladding wall with a number of calculation ring elements and evaluate failure probability for each of the ring element. Then, influence of failure of the ring element on mechanical loads of other ring elements are modeled.

In the recent development of the code in collaboration with Waseda University, it has been indicated that SiC cladded fuel may exhibit intensive PCMI during a loss of coolant accident (LOCA), because there is no cladding ballooning while the fuel pellets thermally expand during LOCA [9]. However, influence of the different models and parameters on the evaluated PCMI characteristics of the fuel was not studied. Namely, the probability threshold at which the calculation ring element is deemed failed and the relaxation parameter on mechanical strength of the failed ring element. Hence, this study aims to reveal influences of such modeling and parameters of FEMAXI-ATF on the evaluation of PCMI of SiC-UO2 during power ramps.

## 2. Calculation method of FEMAXI-ATF

### 2.1. Basic calculation geometry

FEMAXI-ATF analyses a single fuel rod in axisymmetric 1-D coordinate with consideration of the coolant under BWR and PWR conditions. The model of a fuel rod is shown in Fig. 1. A single fuel rod is divided into multiple axial segments. Each segment consists of the pellet, the gap, the cladding and the coolant. The pellet is divided into 36 iso-volume ring elements and cladding into 10 ring iso-thickness elements.

The FEMAXI calculation consists of the thermal calculation in a cylindrical coordinate system and the mechanical calculation by finite element method. In the thermal calculation, the radial temperature distribution and fission gas release are calculated from the input linear heat rate history and heat generation density profile of pellet as a function of rod average burnup. The thermal conductivity and rod surface heat transfer coefficient to coolant are also calculated. Using the calculated temperature profile and fission gas release, thermal expansion and swelling of the pellet and cladding, and the rod internal pressure are determined. They are in turn taken over to the mechanical calculation, where stress and strain, elastic, plastic and creep displacements, and PCMI contact pressure are calculated, and these results are fed back to the thermal calculation through gap thermal conductance. At each timestep, the above iterations are performed until convergence, and the result makes the initial condition for the next time step.

### 2.2. Pseudo-ductility and failure modeling of SiC

In FEMAXI-ATF, microscopic cracks or failures of the fuel cladding elements are not explicitly modeled but influences of such cracks and failures on macroscopic mechanical behavior of the cladding are modeled in a deterministic manner with consideration of statistical distribution of mechanical strengths of mSiC and SiC/SiC.

Fig. 2 illustrates the basic approach of FEMAXI-ATF to model pseudo-ductility and failure of SiC/SiC elements. For SiC/SiC, the stress and strain are assumed to follow a linear relationship until the stress reaches the PLS in the same was as assumed for mSiC. However, unlike metallic materials, PLS of SiC/SiC is statistically distributed. In the mechanical calculation of FEMAXI-ATF, PLS of SiC/SiC is assumed to be distributed with Weibull distribution and the characteristic strength of the distribution is used to represent the PLS in deterministic mechanical calculations [9]. The corresponding strain at PLS is simply determined by assuming a linear stress-strain relationship with the modulus of elasticity (Young's modulus).

For mSiC, the UTS is assumed to be the same as PLS. In the meantime, the difference in UTS and PLS of SiC/SiC is assumed to be distributed with Weibull distribution and the difference is represented by the characteristic strength of the distribution. The corresponding strain at UTS is determined by assuming that the difference in strains at UTS and PLS follow a log normal distribution [9]. Thus, the UTS and PLS points are defined to represent statistically distributing mechanical strengths of mSiC and SiC/SiC.

Beyond the PLS of SiC/SiC, microcracks are generated in the matrix, which is reinforced by the SiC fibers. The resulting pseudo-ductility is represented by Hollomon's curve, for the purpose of modeling the stress-strain relationship beyond PLS of SiC/SiC. The parameters are tuned so that the curve passes through both the PLS and UTS points.

As the stress-strain relationships of mSiC and SiC/SiC are defined deterministically, the failure probabilities of mSiC and SiC/SiC are also evaluated with assumed Weibull distributions. In the present study, any cladding wall element is assumed to have failed when its cumulative failure probability reaches a user defined threshold (e.g., 50 %). Then, modulus of elasticity of the failed cladding wall element is reduced by a relaxation factor to model influence of loss of mechanical strength of the failed element on other cladding wall elements as shown in Fig. 2.

**Table 1**
Moduli of elasticity of different SiC/SiC designs.

| | Modulus of elasticity (GPa) | |
|---|---|---|
| | Radial direction | Axial and circumferential directions |
| SiC/SiC-A | 254 | 213 |
| SiC/SiC–B | 273 | 229 |
| SiC/SiC–C | 210 | 176 |

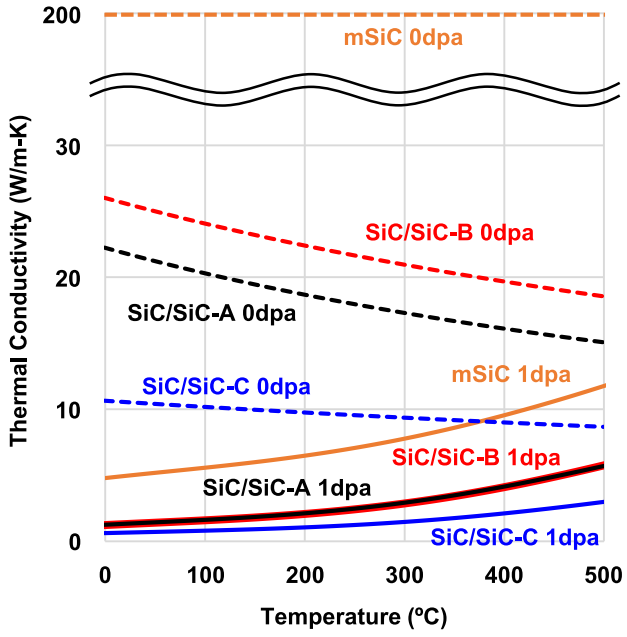


**Fig. 3.** Thermal conductivity models adopted in this study for different SiC designs as functions of temperature and irradiation doses.

## 3. Thermo-physical properties

For simulating PCMI characteristics of SiC-UO2, it is important to select a realistic set of thermo-physical properties of SiC/SiC (as well as for mSiC), because the differences in the CVI methods and fiber designs have large influences not only on the mechanical strength, but also on thermal properties (e.g., thermal conductivity). In this study, SiC/SiC fiber is tentatively assumed as similar to that of Tyranno Fiber (Tyranno SA3/PyC150-A, UBE Corporation) and the thermo-physical properties have been taken from the earlier publication [10]. Some of the important thermo-physical properties assumed in this study are given as follows. The following three designs SA3/PyC150-A, SA3/PyC50-A, HNLS/ML-A have been tentatively selected to cover relatively wide range of the properties, such as the modulus of elasticity and thermal conductivity. Since discussions about comparisons of different SiC/SiC designs are beyond the scope of this study, the selected designs are represented as SiC/SiC-A, -B, and –C, from hereinafter.

### 3.1. Modulus of elasticity and anisotropy

Modulus of elasticity of CVD-mSiC changes with temperature, irradiation induced swelling and porosity as expressed in Eq. (1) by Snead et al. [11]:

$$E = \left[460 \bullet exp(-3.57V_P) - 0.04T \bullet \exp\left(-\frac{962}{T}\right)\right] \bullet (1 - 6.974 \bullet S_{irr}) \quad (1)$$

where, $E$ denotes modulus of elasticity (GPa), $T$ the temperature (K), and $S_{irr}$ the volumetric swelling (ΔV/V). $V_P$ is the porosity, which is expressed by the following equation:

$$V_P = 1 - \frac{\rho_0}{3.21} \quad (2)$$

where, $\rho_0$ denotes initial density (g/cm$^3$). In the present study, pure CVD-mSiC is assumed and the initial density is set as 3210 kg/m$^3$. Hence, the porosity is assumed to be zero.

In the meantime, according to the previous study by Katoh et al. [10], the modulus of elasticity of SiC/SiC drops only by 6 % when the temperature is raised from the room temperature to 1000 °C and influence of irradiation is negligible. Therefore, in this study, it is assumed to be constant and the values available at room temperature are used.

The anisotropy of SiC/SiC is determined by the direction of the fibers, while stress in the cladding is naturally larger in the circumferential and axial directions than that in the radial direction due to the tube geometry. Therefore, in this study, it is assumed that the SiC/SiC fibers are designed in such a way that the moduli of elasticity are relatively small in the direction which is naturally subject to larger stress, because smaller modulus of elasticity leads to smaller stress for a given strain. Namely, the present analysis assumes that moduli of elasticity in the axial and circumferential directions are 84 % of that of the radial direction for different designs as summarized in Table 1. In this study, referring to the treatment in a previous study [6], the shear stress is assumed to be negligible (zero) as follows:

$$\begin{Bmatrix} \sigma_r \\ \sigma_\theta \\ \sigma_z \end{Bmatrix} = \begin{bmatrix} \frac{1-\nu_{\theta z}\nu_{z\theta}}{E_\theta E_z \eta} & \frac{\nu_{\theta r}+\nu_{zr}\nu_{\theta z}}{E_\theta E_z \eta} & \frac{\nu_{zr}+\nu_{\theta r}\nu_{z\theta}}{E_\theta E_z \eta} \\ \frac{\nu_{r\theta}+\nu_{rz}\nu_{z\theta}}{E_z E_r \eta} & \frac{1-\nu_{zr}\nu_{rz}}{E_z E_r \eta} & \frac{\nu_{z\theta}+\nu_{zr}\nu_{r\theta}}{E_z E_r \eta} \\ \frac{\nu_{rz}+\nu_{r\theta}\nu_{\theta z}}{E_r E_\theta \eta} & \frac{\nu_{\theta z}+\nu_{rz}\nu_{\theta r}}{E_r E_\theta \eta} & \frac{1-\nu_{r\theta}\nu_{\theta r}}{E_r E_\theta \eta} \end{bmatrix} \begin{Bmatrix} \varepsilon_r \\ \varepsilon_\theta \\ \varepsilon_z \end{Bmatrix} \quad (3)$$

$$\eta = \frac{1 - \nu_{r\theta}\nu_{\theta r} - \nu_{\theta z}\nu_{z\theta} - \nu_{zr}\nu_{rz} - 2\nu_{r\theta}\nu_{\theta z}\nu_{zr}}{E_r E_\theta E_z} \quad (4)$$

$$\frac{\nu_{r\theta}}{E_r} = \frac{\nu_{\theta r}}{E_\theta}, \frac{\nu_{rz}}{E_r} = \frac{\nu_{zr}}{E_z}, \frac{\nu_{z\theta}}{E_z} = \frac{\nu_{\theta z}}{E_\theta} \quad (5)$$

where, σ_(r/θ/z) denotes radial/circumferential/axial stress (Pa), E moduli of elasticity (Pa), and $\nu$ Poisson's ratio. The Poisson's ratios are set as: $\nu_{r\theta} = 0.16, \nu_{z\theta} = 0.13, \nu_{rz} = 0.16$.

### 3.2. Irradiation induced swelling

Although some limited irradiation data indicate smaller irradiation induced swelling of CVI-SiC/SiC than that of CVD-mSiC (Newsome et al. [12]), other data indicate no significant difference [10]. Hence, in this study, the following model is used for both mSiC and SiC/SiC (Katoh et al.). The volumetric swelling increases with the fast neutron fluence until it reaches saturation at about 1 dpa (about $10^{25}$ n/m$^2$, E > 1 MeV). The saturation level decreases as the irradiation temperature is increased.

$$\dot{S}_{irr} = k_s \bullet \gamma^{-\frac{1}{3}} \bullet \exp\left(-\frac{\gamma}{\gamma_{SC}}\right) \quad (6)$$

where, $\dot{S}_{irr}$ denotes swelling ratio (ΔV/V), and $\gamma$ the displacement damage dose (dpa). Also, $k_s$ and $\gamma_{SC}$ are temperature-dependent factor and characteristic displacement damage dose (dpa) respectively:

$$k_S = 0.10612 - 1.5904 \times 10^{-4}T + 6.0631 \times 10^{-8}T^2 \quad (7)$$

$$\gamma_{SC} = 0.51801 - 2.7651 \times 10^{-3}T + 9.4807 \times 10^{-6}T^2 - 1.3095 \times 10^{-8}T^3 + 6.7221 \times 10^{-12}T^4 \quad (8)$$

**Table 2**
Distribution parameters for SiC.

| | Weibull modulus $n$ | Characteristic strength $\sigma_0$ (MPa) |
|---|---|---|
| SiC/SiC PLS | 10.5 | 171 |
| SiC/SiC difference between UTS and PLS | 4.1 | 211 |
| mSiC fracture stress | 4.5 | 370 |

PLS, proportional limit stress; UTS, ultimate tensile strength.

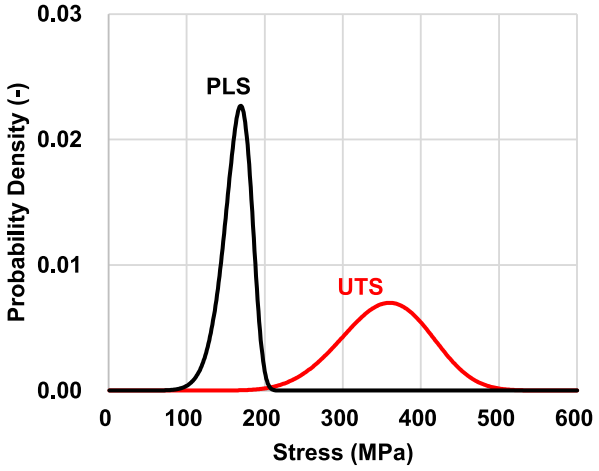


**Fig. 4.** Weibull distribution of SiC/SiC PLS and UTS.

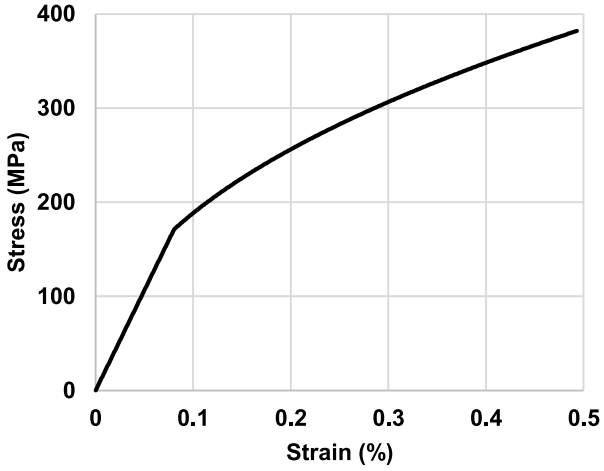


**Fig. 5.** Example of the stress-strain curve of SiC/SiC (Modulus of elasticity: 213 (GPa), K = 4014 (MPa), and n = 0.4428).

**Table 3**
9 by 9 BWR fuel design.

| | |
|---|---|
| Maximum linear heat rate (kW/m) | 44.0 |
| Pellet diameter (mm) | 9.4 |
| Pellet density (%TD) | 97 |
| Cladding outer diameter (mm) | 11.0 |
| Cladding wall thickness (mm) | 0.70 |
| Pellet-cladding diameter gap (mm) | 0.20 |
| Active fuel length (m) | 3.71 |
| Filled gas/filler pressure (MPa) | He/1.0 |

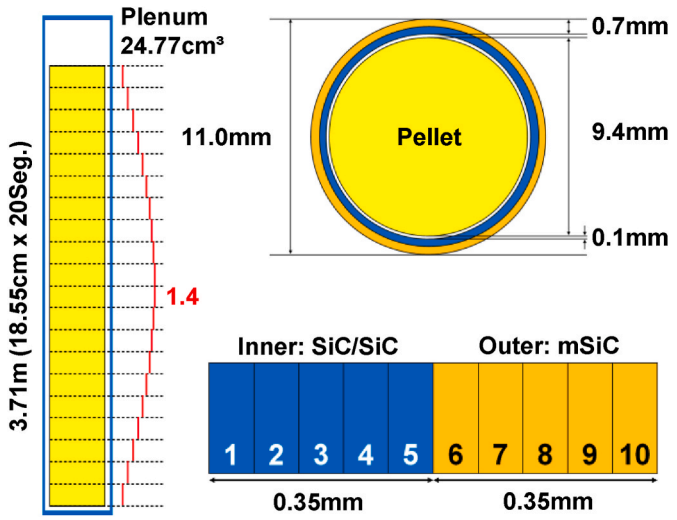


**Fig. 6.** The fuel rod dimensions and the calculation element divisions of the SiC cladded fuel rod.

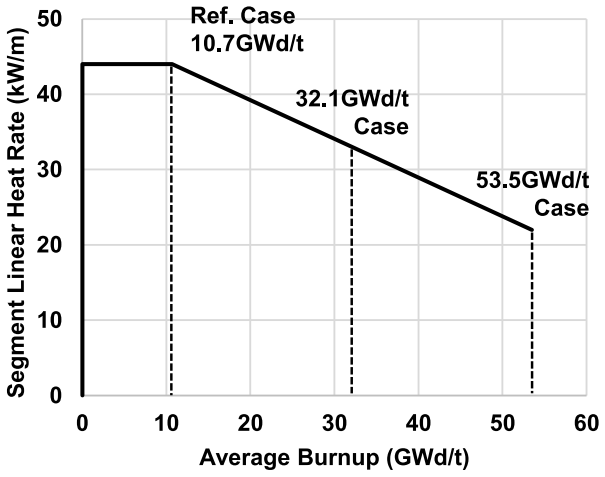


**Fig. 7.** The peak power segment linear heat rate (LHR) against the rod average burnup assumed as the irradiation history of the normal operation.

### 3.3. Thermal conductivity

The thermal conductivity of CVD-mSiC decreases significantly due to irradiation swelling. It is expressed by the following Eq. (6), which is given by Snead et al. [11]:

$$\lambda = \frac{1}{0.0595 \bullet S_{irr} \bullet 100 + 0.005} \tag{9}$$

where, $\lambda$ denotes thermal conductivity (W/m/K), and $S_{irr}$ the volumetric swelling (ΔV/V).

The thermal conductivity of SiC/SiC is lower than that of mSiC when unirradiated and becomes even lower upon irradiation. It depends on the manufacturing process, and much lower in CVI-HNLS than CVI-SA3. In this study, the following three different cases are modeled:

$$\mathrm{SiC/SiC\text{-}A}: \lambda = \frac{1}{\left(0.18 - 1.3\times10^{-4}T\right)\bullet\left(S_{irr}\bullet100\right)^2 + 0.033307 + 4.2751\times10^{-5}T} \tag{10}$$

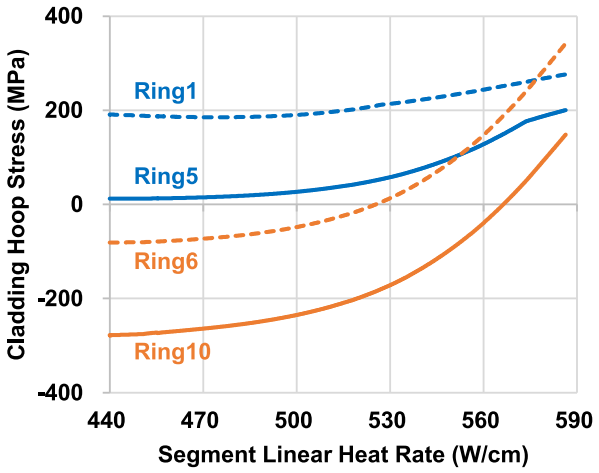


**Fig. 8.** The cladding ring element hoop stresses of the peak power fuel segment during the power ramp for the reference case (average burnup: 10.7 GWd/t).

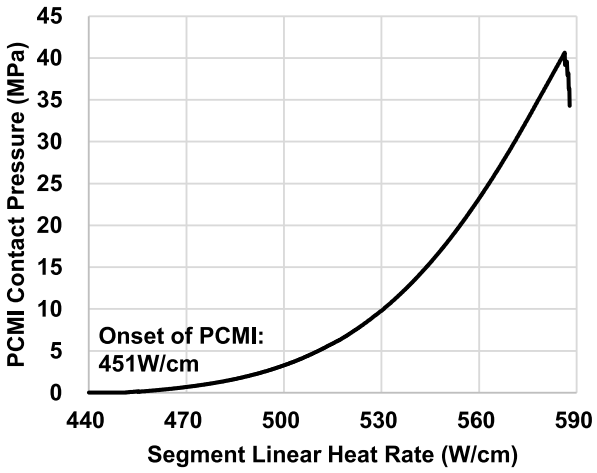


**Fig. 10.** The PCMI contact pressure during the power ramp for the reference case (average burnup: 10.7 GWd/t).

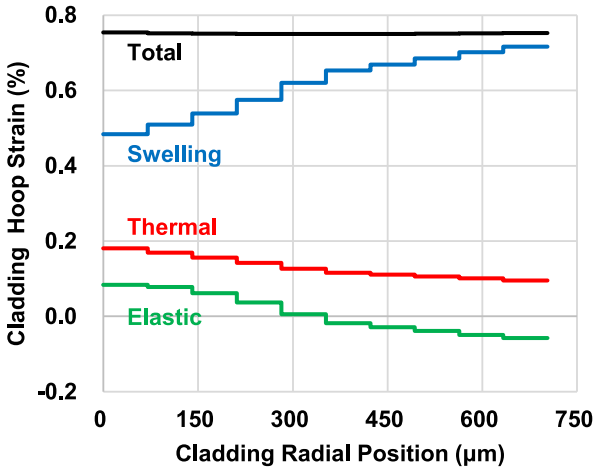


**Fig. 9.** The radial distributions of cladding hoop strains at the beginning of the power ramp for the reference case (average burnup: 10.7 GWd/t).

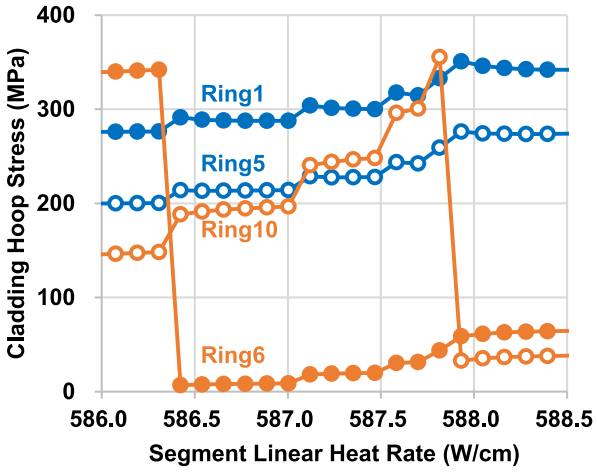


**Fig. 11.** The cladding ring element hoop stresses of the peak power fuel segment during the power ramp for the reference case (average burnup: 10.7 GWd/t, near the failure LHR).

$$\mathrm{SiC/SiC-B}:\lambda=\frac{1}{\left(0.18-1.2\times10^{-4}T\right)\bullet\left(S_{\mathrm{irr}}\bullet100\right)^{2}+0.030023+3.0913\times10^{-5}T} \tag{11}$$

$$\mathrm{SiC/SiC-C}:\lambda=\frac{1}{\left(0.37-2.7\times10^{-4}T\right)\bullet\left(S_{\mathrm{irr}}\bullet100\right)^{2}+0.082412+4.3072\times10^{-5}T} \tag{12}$$

where, $\lambda$ denotes thermal conductivity (W/m/K), and $S_{\mathrm{irr}}$ the volumetric swelling (ΔV/V).

The temperature dependences of these thermal conductivities are shown in Fig. 3. Note that the 0 dpa line represents the value at the unirradiated point, and the 1 dpa line represents the final value at the point when the irradiated swelling has almost reached saturation.

### 3.4. Mechanical strength

The mechanical strengths of SiC are statistically distributed, which are often described by the Weibull distribution:

$$f(\sigma)=\frac{n}{\sigma_0}\left(\frac{\sigma}{\sigma_0}\right)^{n-1}\exp\left\{-\left(\frac{\sigma}{\sigma_0}\right)^{n}\right\} \tag{13}$$

where, $\sigma$ denotes stress (MPa), $n$ the Weibull modulus. Also, $\sigma_0$ is the characteristic strength. This stress is $1-\mathrm{e}^{-1}\approx63\%$ in the cumulative distribution Eq. (11) integrating the probability density distribution function.

$$F(\sigma)=1-\exp\left\{-\left(\frac{\sigma}{\sigma_0}\right)^{n}\right\} \tag{14}$$

The SiC distribution parameters used in this study are the same as those used in the previous study [4]. These values are summarized in Table 2. The distribution parameters also depend on the SiC/SiC manufacturing process, but these common values are tentatively used in this study.

To obtain the cumulative distribution of SiC/SiC UTS, the probability density distribution of PLS is first expressed as follows:

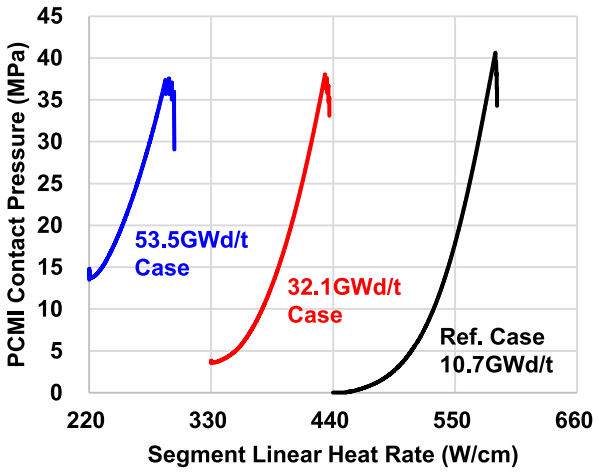


**Fig. 12.** The PCMI contact pressure during the power ramps for the different burnup cases (average burnup: 10.7 GWd/t, 32.1 GWd/t, and 53.5 GWd/t).

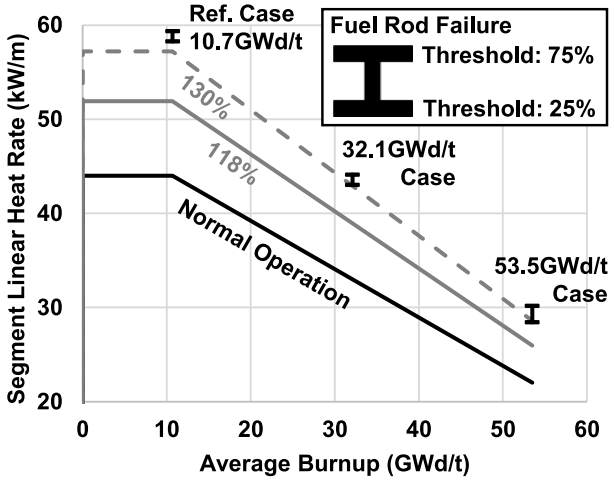


**Fig. 13.** Powers at the fuel rod failures and the peak power segment linear heat rate against the rod average burnup.

$$g(\sigma)=\frac{10.5}{171}\left(\frac{\sigma}{171}\right)^{9.5}\exp\left\{-\left(\frac{\sigma}{171}\right)^{10.5}\right\} \tag{15}$$

Furthermore, the probability density distribution of the difference between PLS and UTS is expressed as follows:

$$f(\sigma)=\frac{4.1}{211}\left(\frac{\sigma-\sigma_p}{211}\right)^{3.1}\exp\left\{-\left(\frac{\sigma-\sigma_p}{211}\right)^{4.1}\right\} \tag{16}$$

where, $\sigma_p$ denotes PLS (MPa), and its distribution follows Eq. (13). Accordingly, the probability density distribution of the SiC/SiC UTS is integrated over the range of PLS values and is expressed as follows:

$$f(\sigma)=\int\frac{4.1}{211}\left(\frac{\sigma-y}{211}\right)^{3.1}\exp\left(-\left(\frac{\sigma-y}{211}\right)^{4.1}\right)g(y)dy \tag{17}$$

The probability density distribution of PLS and UTS for SiC/SiC is shown in Fig. 4.

### 3.5. SiC/SiC pseudo-ductility

The pseudo-ductility of SiC/SiC is taken into account in creating the stress-strain curve in the form of the Hollomon type equation.

$$\sigma = K \bullet \varepsilon^n \tag{18}$$

Here, four values of stress/strain at the proportional limit and at failure, respectively, are needed to create the stress-strain curve. In this study, the characteristic strengths of the Weibull distribution are used for this PLS and UTS. The proportional limit strain is obtained from the circumferential Young's modulus of SiC/SiC and the characteristic parameters of PLS. In addition, the strain difference between UTS and PLS was set to 0.4128 % [4]. The stress-strain curve obtained by this procedure is shown in Fig. 5, where K = 4014 (MPa), and $n$ = 0.4428.

## 4. Analysis conditions

### 4.1. Fuel rod design

The 9 by 9 BWR design specifications were assumed for the fuel rods as summarized in Table 3. The present analytical model geometry of a fuel rod is shown in Fig. 6. The fuel rod is divided into 20 axial segments. In addition, the fuel pellet and the cladding are divided into 36 iso-volume ring elements and 10 iso-thickness ring elements, respectively.

According to one of the analytical studies under normal PWR operation condition, a cladding wall design with 4: 6 thickness ratio of the inner SiC/SiC and the outer mSiC layer show the best performance [13]. However, the study did not consider PCMI and optimization of the cladding design is beyond the scope of the current study. Hence, a

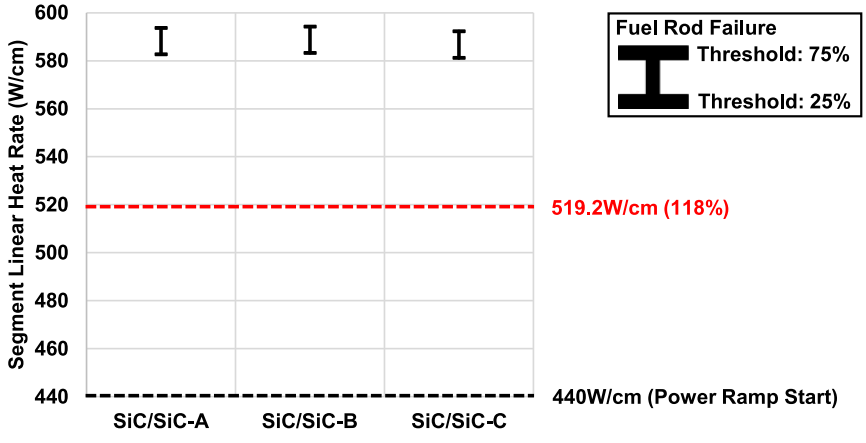


**Fig. 14.** Powers at the fuel rod failures of the three SiC/SiC designs with different moduli of elasticity for the reference burnup case (average burnup: 10.7 GWd/t).

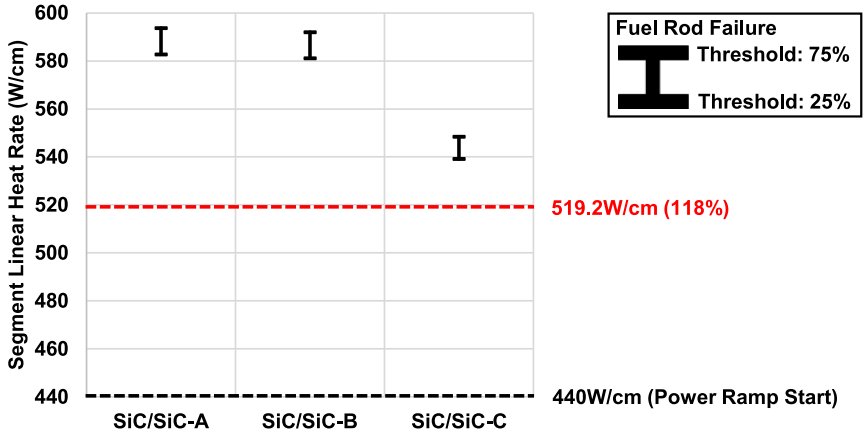


**Fig. 15.** Powers at the fuel rod failures of the three SiC/SiC designs with different thermal conductivities for the reference burnup case (average burnup: 10.7 GWd/t).

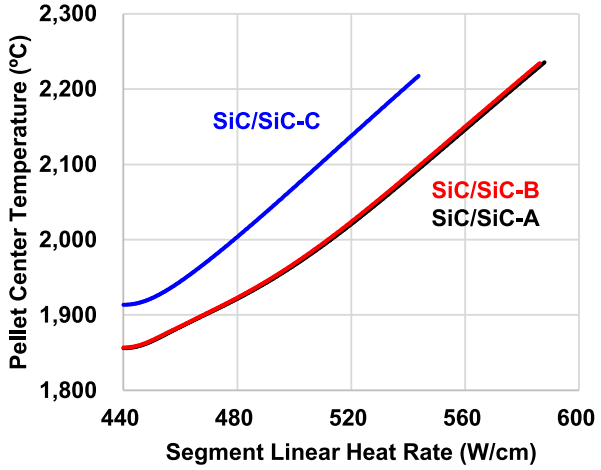


**Fig. 16.** Pellet centerline temperatures during the power ramps of the three SiC/SiC designs with different thermal conductivities for the reference burnup case (average burnup: 10.7 GWd/t).

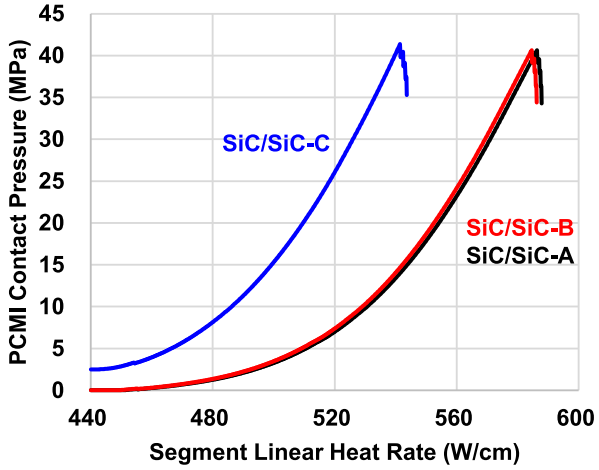


**Fig. 17.** PCMI contact pressures during the power ramps of the three SiC/SiC designs with different thermal conductivities for the reference burnup case (average burnup: 10.7 GWd/t).

tentative cladding wall design with the thickness ratio of 1: 1 for the inner SiC/SiC and the outer mSiC layers is adopted in this study.

### *4.2. Irradiation history*

A test power ramp case has been tentatively determined with a design power history as shown in Fig. 7. The Peak power indicates the power history at the tenth calculation segment from the bottom of the fuel stack. It is assumed that the peak power of 44.0 kW/m continues until the rod average burnup reaches 10.7 GWd/t. Then, the power is assumed to linearly decrease until the rod average discharge burnup reaches 53.5 GWd/t. Then, power ramps were assumed at different burnups. Namely, power ramps were assumed when the rod average burnup reached 10.7 GWd/t (for the reference case), 32.1 GWd/t and 53.5 GWd/t. For all cases, a constant power ramp rate of 0.41 %/s was assumed by referring to the uncontrolled control rod withdrawal at normal operation of BWR. A continuous power increase at the given rate was hypothetically assumed until the fuel rod failure.

## 5. Analysis results

The transition of the cladding circumferential stress in the axial segment #10 during the power ramp for the reference case is shown in Fig. 8. It may be worth noting that the basic nature of SiC cladding is that the neutron irradiation swelling induces tensile stress in the inner wall while it induces compressive stress in the outer wall, because the irradiation saturation level decreases with increasing temperature (i.e., larger swelling in the outer wall than the inner wall) [6]. It means that SiC cladding is generally subject to such stress conditions (tensile in the inner wall and compressive in the outer wall) without any external forces. Then, the thermal stress and PCMI contact pressure induces additional stresses during the power transient. At the start of the power ramp, the stresses in the inner SiC/SiC layer (rings 1 through 5) are tensile while those of the outer mSiC layer (rings 6 through 10) are compressive. At the start of the power ramp of the reference case (10.7 GWd/t), the pellet-cladding gap is still open and there is no PCMI. Hence, the initial stress profile can be understood from the differences in the irradiation swelling across the wall thickness direction and the transient stress profile changes can be understood from the differences in thermal expansion across the wall during the power ramp. Initially,

just before the power ramp, the irradiation swelling of the outer most ring element (0.72 %) is larger than that of the inner most ring element (0.48 %), because the irradiation saturation level decreases with increasing temperature. Such difference in the swelling across the cladding wall thickness direction is the main cause of the tensile stress in the inner wall and the compressive stress in the outer wall. To clarify this point, Fig. 9 shows the total strain, the irradiation swelling, the thermal and the elastic strains in the cladding circumferential direction of the axial segment #10 (the creep and plastic strains are effectively zero). As shown in Fig. 9, the outer wall is trying to expand more than the inner wall because of larger swelling. As the power ramp starts, the larger thermal expansion of the inner wall (ring 1) than that of the outer wall (ring 10), as indicated in Fig. 9, leads to slight reductions of the tensile stress of the inner wall and compressive stress of the outer wall, respectively. Then, as the power ramp continues, thermal expansion of the fuel pellet leads to onset of PCMI as shown in Fig. 10, which induces rapid change of the stress in the mSiC layer from compressive to tensile. Further increase in the PCMI contact pressure also increased tensile stresses in the SiC/SiC ring elements.

Next, the circumferential stresses of the different cladding ring elements are shown in Fig. 11 around the moment when the outer mSiC ring elements failed. In this case, the cladding failure began from the innermost ring element of the outer mSiC layer. At the time of the failure, the modulus of elasticity of the failed element (Ring 6) is relaxed. As the result, circumferential stress in Ring 6 is reduced to almost zero, while the stress in the other ring elements increased stepwise. In this manner, the cladding ring element failures propagated from the inside of the mSiC layer to the outside until all the mSiC ring elements have failed.

It should be noted that in the current analyses, the relaxation factor on modulus of elasticity of the failed cladding ring element cannot be set as zero to avoid numerical instability at the moment of the failure. It is tentatively determined as 0.21 and this is why the stress does not become exactly zero at the moment of the failure and it continues to increase even after the failure. Hence, the current analysis results may be underestimating propagations of failures of the cladding wall ring elements across the thickness direction. It should also be noted that the current study is still limited to mechanistic modeling of SiC failure as it only models the propagation of the cladding wall element failure across the homogeneous continuum wall without considering generations and propagations of cracks. In particular, the initiation of crack is expected to lead to a spontaneous propagation of crack (i.e., a catastrophic failure) in the mSiC layer, while such propagation may be suppressed in the SiC/SiC layer to some extent, due to the fibers. However, the results in Fig. 11 show that even with such continuum cladding wall modeling, the failure propagation occurs within very narrow power range during the power ramp. The results indicate that initiation of the failure at the inner most element of the mSiC layer may be practically regarded as failure of the entire mSiC layer.

PCMI contact pressures during the power ramps at different rod average burnups are shown in Fig. 12. In all cases, PCMI relaxations due to cladding failures occur when the contact pressures reach about 38 MPa. These results indicate fuel rod failures by PCMI during the power ramps.

In addition, the powers at failures of all the analyzed cases are summarized in Fig. 13. For each case, the power range of failures are evaluated by using different probability thresholds at which the cladding ring element is regarded as failed. Namely, for the case with 25 % and 75 % failure probabilities. The 118 % rated power line indicates a tentative reference for the peak power during uncontrolled withdrawal of control rods at normal operation. The results indicate predicted fuel rod failures occur when the power exceeds 130 % of the rated power level. However, it should be stressed that predicting the failure power is beyond the scope of the present work. For such predictions, more sensitivity analyses are necessary, which may influence the predicted fuel rod failures. The obvious and important limitation of the current study is the continuum cladding wall modeling, which cannot consider crack generations and propagation of the cracks. Considering the nature of fuel performance modeling codes, one of the realistic ways to consider such crack propagation effect may be to incorporate some failure acceleration parameter, which enhances failure probability of the cladding wall element, when its adjacent element is determined to have failed. The calculation ring element thickness or calculation resolution of the cladding wall may also influence the failure propagation. Furthermore, such analyses should address not only the uncertainties of thermo-mechanical properties of mSiC and SiC/SiC as partially discussed in this study, but also those of UO2 pellet modeling may also have significant impact on the predicted PCMI behavior of SiC– UO2 (e.g., pellet densification, swelling, creep).

A comparison of the power at failures at the segment #10 with different moduli of elasticity of SiC/SiC are shown in Fig. 14. The results indicate small differences due to differences in moduli of elasticity of SiC/SiC.

Finally, Fig. 15 compares the power at failure in the sensitivity analysis for SiC/SiC thermal conductivity. The failure is caused much earlier in the SiC/SiC–C case with relatively low thermal conductivity. This is because the lower thermal conductivity of SiC/SiC–C leads to higher fuel pellet temperature (as shown in Fig. 16), which leads to larger thermal expansion of the pellet and larger PCMI contact pressure (as shown in Fig. 17).

## 6. Conclusions

FEMAXI-ATF is being developed with a focus on evaluation of the PCMI behavior of SiC cladded fuel. The cladding wall is divided into a number of calculation ring elements. Failure of any of the ring element is determined from the failure probability, evaluated from the Weibull distribution of mSiC and SiC/SiC. This study showed that the threshold cumulative probability at which the ring element is assumed to have failed has limited influence on the evaluated PCMI failure power of the SiC cladded fuel during power ramp for the range between 25 % and 75 % cumulative failure probability. Then, when the modulus of elasticity of the failed element was reduced to 21 % of the original value, the stress on the failed element could be reduced close to zero. However, reducing the relaxation factor to smaller value induced numerical instability. Further development may be necessary to address limitation of the continuum cladding wall modeling to consider crack propagation, influence of the calculation resolution of the cladding wall and optimize parameters for evaluation of PCMI behavior of SiC cladded fuel.

## Declaration of competing interest

The authors declare that they have no known competing financial interests or personal relationships that could have appeared to influence the work reported in this paper.

## Acknowledgements

This work was partly supported by JSPS KAKENHI Grant Number 20H02669. A part of this study is the result of “Understanding Mechanisms of Severe Accidents and Improving Safety of Nuclear Reactors by Computer Science” of Waseda Research Institute for Science and Engineering and the authors acknowledge support of the Institute for Advanced Theoretical and Experimental Physics, Waseda University.

## References

[1] State-of-the-Art Report on Light Water Reactor Accident-Tolerant Fuels, OECD Nuclear Energy Agency, 2018.
[2] B.A. Pint, K.A. Terrani, M.P. Brady, T. Cheng, J.R. Keiser, High temperature oxidation of fuel cladding candidate materials in steam–hydrogen environments, J. Nucl. Mater. 440 (2013) 420–427.
[3] Y. Katoh, K.A. Terrani, Systematic Technology Evaluation Program for SiC/SiC Composite-Based Accident-Tolerant LWR Fuel Cladding and Core Structures:

Revision 2015", Oakridge National Laboratory, August 2015. ORNL/TM-2015/454.
[4] J.G. Stone, et al., Stress analysis and probabilistic assessment of multi-layer SiC-based accident tolerant nuclear fuel cladding, J. Nucl. Mater. 466 (2015) 682–697.
[5] C. Yin, Study on the thermal-mechanical performance of SiC composites cladding under multiple conditions, Paper 16793, Proc. ICONE 2020 (Virtual, Online) (2020).
[6] G. Singh, et al., Thermo-mechanical assessment of full SiC/SiC composite cladding for LWR applications with sensitivity analysis, J. Nucl. Mater. 499 (2018) 126–143.
[7] N. Shirasu, H. Saito, S. Yamashita, F. Nagase, Fuel behavior analysis for accident tolerant fuel with SiC cladding using adapted FEMAXI-7 code. Proc. 2017 Water Reactor Fuel Performance MeetingJeju, Korea, 2017.
[8] M. Suzuki, H. Saitou, Y. Udagawa, et al., Light Water Reactor Fuel Analysis Code FEMAXI-7 (Models and Structure)", JAEA-Data/Code 2013-005, 2013.
[9] Y. Nakao, A. Yamaji, Y. Nemoto, S. Yamashita, PCMI analysis of the SiC cladded fuel during BWR LOCA with FEMAXI-ATF. Proc. Topfuel 2022, Raleigh, USA, 2022, pp. 334–342.
[10] Y. Katoh, et al., Continuous SiC fiber, CVI SiC matrix composites for nuclear applications: properties and irradiation effects, J. Nucl. Mater. 448 (2014) 448–476.
[11] L.L. Snead, et al., Handbook of SiC properties for fuel performance modeling, J. Nucl. Mater. 371 (2007) 329–377.
[12] G. Newsome, et al., Evaluation of neutron irradiated silicon carbide and silicon carbide composites, J. Nucl. Mater. 371 (2007) 76–89.
[13] Y. Lee, et al., Design optimization of multi-layer Silicon Carbide cladding for light water reactors, Nucl. Eng. Des. 311 (2017) 213–223.